Geochemistry, Geophysics, Geosystems

RESEARCH ARTICLE
10.1029/2018GC007609

Key Points:
- Crystallization pressure of CaO hydration exceeds 27 MPa at 1-km crustal depth
- Fluid transport via capillary flow is rate limiting
- Strain rate exhibits negative, power law dependence on uniaxial load

Supporting Information:
- Supporting Information S1
- Table S2
- Table S3

Correspondence to:
S. Lambart,
sarah.lambart@utah.edu

Citation:
Lambart, S., Savage, H. M., Robinson, B. G., & Kelemen, P. B. (2018). Experimental investigation of the pressure of crystallization of $Ca(OH)_2$: Implications for the reactive cracking process. *Geochemistry, Geophysics, Geosystems*, *19*. https://doi.org/10.1029/2018GC007609

Received 13 APR 2018
Accepted 15 AUG 2018
Accepted article online 30 AUG 2018

Experimental Investigation of the Pressure of Crystallization of $Ca(OH)_2$: Implications for the Reactive Cracking Process

S. Lambart[1,2], H. M. Savage[1], B. G. Robinson[1], and P. B. Kelemen[1]

[1]Lamont-Doherty Earth Observatory, Columbia University, Palisades, NY, USA, [2]Geology and Geophysics, University of Utah, Salt Lake City, UT, USA

Abstract Mineral hydration and carbonation can produce large solid volume increases, deviatoric stress, and fracture, which in turn can maintain or enhance permeability and reactive surface area. Despite the potential importance of this process, our basic physical understanding of the conditions under which a given reaction will drive fracture (if at all) is relatively limited. Our hydration experiments on CaO under uniaxial loads of 0.1 to 27 MPa show that strain and strain rate are proportional to the square root of time and exhibit negative, power law dependence on uniaxial load, suggesting that (1) fluid transport via capillary flow is rate limiting and (2) decreasing strain rate with increasing confining pressure might be a limiting factor in reaction driven cracking at depth. However, our experiments also demonstrate that crystallization pressure due to hydration exceeds 27 MPa (consistent with a maximum crystallization pressure of 153 MPa for the same reaction, Wolterbeek et al., https://doi.org/10.1007/s11440-017-0533-5). As a result, full hydration can be achieved at crustal depths exceeding 1 km, which is relevant for engineered fracture systems.

1. Introduction

Retrograde metamorphism is an essential process of geodynamics. Hydration of igneous, oceanic crust and mantle (Craft & Lowell, 2009; Roland et al., 2010; Van Avendonk et al., 2011), followed by subduction (Carlson & Miller, 2003; Gorman et al., 2006), supplies significant volumes of water that drive arc volcanism (Schmidt & Poli, 1998; Sobolev & Chaussidon, 1996), controls the rheology of oceanic plate boundaries (Hirauchi et al., 2016), and lubricates convection by maintaining or increasing the hydrogen content of the mantle over time (McGovern & Schubert, 1989). Chemical weathering is as important as magmatism and plate tectonics in shaping the Earth's surface (Fletcher et al., 2006; Jamtveit et al., 2009). Mineral carbonation during alteration of ultramafic and mafic rocks throughout the plate tectonic cycle is increasingly recognized as an important but poorly characterized link in the carbon cycle (Dessert et al., 2003; Kelemen & Manning, 2015). Finally, engineered methods emulating this natural process are potentially transformational technologies for extraction of oil and gas from *tight* reservoirs, managing the permeability of wells, facilitating or enhancing circulation of water in geothermal power generation systems, in situ solution mining, for example, for Uranium, and in situ geologic carbon capture and storage (Kelemen & Matter, 2008; Matter et al., 2016; Wolterbeek et al., 2017).

Despite the potential importance of reaction-driven cracking, fundamental uncertainties remain in methods for estimating crystallization pressures during retrograde metamorphism. Generation of stress due to crystallization has been mostly studied in environments where crystallization occurs within a porous medium whose matrix does not participate in the reaction. For instance, deterioration in building stones due to the crystallization of salt is particularly well documented with numerous experimental (e.g., Derluyn et al., 2014; Noiriel et al., 2010; Steiger, 2005) and theoretical (e.g., Coussy, 2006; Osselin et al., 2014) studies attempting to quantify the stresses involved. During mineral hydration or carbonation, however, the matrix supplies reactive components via dissolution and reprecipitation (Putnis, 2009). In either case, generation of crystallization pressure, that is, the deviatoric stress in excess of confining pressure, depends on the degree of supersaturation and the change of molar volume between the dissolving and precipitating phases (Kelemen et al., 2011; Kelemen & Hirth, 2012). However, the actual pressure generated in a rock undergoing retrograde metamorphism also depends on many other factors, including the rate of viscous deformation, formation of fractures, friction along preexisting fractures, shear heating combined with thermal diffusion, the potential for compaction, clogging of porosity, and armoring of reactive surfaces

with product phases. As a result, there is no consensus regarding the nature of deformation due to retrograde metamorphism (e.g., Ghofrani & Plack, 1993; Kuleci et al., 2017; Ostapenko & Yaroshenko, 1975; Skarbek et al., 2018; Van Noort et al., 2017; Wolterbeek et al., 2017; Zhu et al., 2016). Moreover, it has been suggested that the upper bound of stress generated by reaction depends on the bulk pore pressure (Rahman & Grasley, 2017), the pore structure (Lee & Kurtis, 2017), and/or surface and interfacial properties between the porous solid matrix, the growing crystal, and the fluid phase (Espinosa-Marzal & Scherer, 2010; Kelemen et al., 2013; Røyne & Jamtveit, 2015; Shahidzadeh-Bonn et al., 2008; Steiger, 2005; Zheng et al., 2018; and references therein). Kelemen and Hirth (2012) developed thermodynamic and mineral physics methods to estimate crystallization pressure during hydration and carbonation of the abundant rock-forming mineral olivine. Assuming that the crystallization pressure is limited by available chemical potential energy, they suggest two possible simple formulations:

$$P' = -\frac{\Delta G_r}{\Delta V_s} \tag{1}$$

and

$$P' \leq -\frac{\Delta G_r}{\Delta V_s} + \frac{P\Delta V_r}{\Delta V_s}, \tag{2}$$

where P' is the crystallization pressure, ΔG_r is the Gibbs free energy of a reaction, ΔV_s is the change in solid volume resulting from this reaction, ΔV_r is the volume change of the stoichiometric reaction (including fluid), and P is the confining pressure. (Also, see Fletcher & Merino, 2001, Steiger, 2005, and Wolterbeek et al., 2017, for similar formulations). The inequality arises because equation (2) is derived with the assumption (implicit in prior work) that all available chemical potential energy is converted into work. Using equation (2), P' is on the order of 500 MPa for olivine hydration and carbonation at 200 °C. Kelemen and Hirth (2012) also developed a relationship between P' and the density of fractures formed by expansion during olivine hydration at ~200–300 °C, which also yields P' of ~300 MPa. Based on these estimates, which are higher than the differential stress required to fracture rocks (e.g., Attewell & Farmer, 1976), it may be possible for the volume change due to olivine hydration and carbonation to cause fracture formation and dilation, maintaining or increasing permeability and reactive surface area in a positive feedback mechanism. However, both the thermodynamic and physical estimates of P' remain highly uncertain. Moreover, this thermodynamic expression does not incorporate energy sinks such as exothermic heating, frictional heating, and/or thermal diffusion. Finally, thermodynamically calculated pressures from equation (2) provide an upper bound that commonly exceeds stresses required for rock failure, via fracture, frictional sliding on existing fractures, closing of nanofilms that allow crystal growth when disjoining pressure is exceeded, and/or viscous flow (e.g., pressure solution, as noted by Kelemen & Hirth, 2012, and references therein).

2. Materials and Methods

To explore the effect of confining pressure on volume changes during retrograde metamorphism, and ultimately provide a better estimation of the relationships between P', chemical potential, and confining pressure, we explored crystallization pressure in a simple system, the hydration of quicklime (CaO) to form portlandite ($Ca(OH)_2$) under laboratory conditions:

$$\text{solid CaO} + H_2O = \text{solid } Ca(OH)_2. \tag{3}$$

The hydration of calcium oxide is a good analog for forsterite carbonation, with faster reaction rates but similar solid volume changes (96% and 84% in stoichiometric proportions), assuming densities of 3.34 and 2.25 g/cm^3 for CaO (Haynes, 2011) and portlandite (Taylor, 1997), and 3.22, 2.65, and 2.96 g/cm^3 for forsterite (e.g., Kumazawa & Anderson, 1969), silica (Haynes, 2011), and magnesium carbonate (e.g., Kornprobst & Plank, 2013), respectively, and ΔG_r(25 °C) (-57 and -70 kJ/mol) for CaO hydration and olivine carbonation, respectively (see Text S1 in the supporting information for details on calculations). Using equation (2), $P'_{Ca(OH)_2} \leq 3.5$ GPa at 25 °C and 0.1 MPa on the same order of magnitude as P' estimated for olivine hydration and carbonation in the same conditions. These crystallization pressures are 2 to 3 orders of

magnitude larger than the tensile strength for igneous rocks (5–30 MPa; e.g., Cai, 2010; Lumb, 1983; Schultz, 1995) and at least an order of magnitude larger than the compressive strength of igneous rocks (Attewell & Farmer, 1976).

Reagent $CaCO_3$ powder (99.5% purity and average size of 10 μm) was used as a starting material. The powder was decarbonated at 850 °C for 2 hr and cooled under vacuum, before being cold pressed at 6,500 psi for one half-inch-diameter samples and at 3,500 psi for 5-mm-diameter samples to form cylinders with initial porosity Φ_0, ranging from 0.38 to 0.53. Conditions were chosen to minimize the sintering effect and maximize the reactivity of the CaO powder (see Text S2 in the supporting information; Borgwardt, 1989; Shin et al., 2009).

Initial porosities were calculated such as

$$\Phi_0 = 1 - \frac{m_0/\rho}{V_0} \tag{4}$$

with m_0 (in grams) and V_0 (in cubic centimeters), the mass and volume of the cylinder, respectively, and ρ the density of the material. Precision of length and initial weight measurements are ±0.005 cm and ± 0.1 mg, respectively (Table 1). Once formed, these cylinders were baked again for 30 min at 850 °C—to ensure that all $CaCO_3$ and/or $Ca(OH)_2$ that might have been produced during contact with air during the cold pressing process was dehydrated to form CaO—and then cooled under vacuum for ~30 min. The samples were prepared immediately before each experiment to minimize the contact of the cylinders with air before the experiment.

Using experimental methods similar to those of Wolterbeek et al. (2017), we conducted experiments in which the cylinder of cold-pressed CaO powder was confined in hardened steel and subject to a constant uniaxial load, σ (between 0.1 and 27.2 MPa), while water was introduced through a 10-μm porous frit at the bottom of the sample (Figure 1). Preliminary tests performed with a 20-μm porous frit showed some extruded material inside the frit at the end of the experiment, suggesting the resulting $Ca(OH)_2$ grains are between 10- and 20-μm diameters. We note however that the extruded material did not significantly block flow through the frit. The interior of the die was covered with a thin film of electrical insulating compound; this hydrophobic grease does not react with the CaO and suppresses adhesion of the material to the steel. Without lubrication, the reacted material did not expand vertically and the porosity of the cylinder dropped significantly. We recorded the displacement of the piston using either a dial indicator or a linear variable differential transformer and assumed that the effect of friction is negligible.

All but two experiments were conducted at room temperature (~22 °C). The two additional experiments were performed at ~55 °C by placing a band heater around the pressure vessel. Temperature was monitored in selected experiments with a thermocouple placed at the top of the die (Figure 1a). The temperature variation was less than ±3 °C. Once the experiments stopped, the wet cylinders were weighed and then dried (Figure 1b). We first chose to dry samples at 100 °C under vacuum, but three samples showed evidence for continuation of the reaction (deformation of the cylinder) inside the furnace. Hence, we then dried the samples at 200 °C for 1 hr. No evidence of continuation of the reaction was observed in these conditions. Table 1 summarizes the experimental conditions and results.

3. Results

We emphasize three key observations. In addition, we briefly discuss possible reasons for variability in the results of repeat experiments with the same initial conditions.

3.1. Positive Volume Change in all Experiments

A positive volume change is observed in all experiments (Figure 2a), indicating that the crystallization pressure (equation (2)) for hydration of quicklime to form portlandite (equation (3)) is higher than the maximum axial load (27.2 MPa). This is the case despite the relatively high initial porosity of the samples (Φ_0 = 0.36 to 0.52; Table 1). Final porosity is >0.05 in all samples (Table 1), and reaction was more than 80% complete in most experiments. For comparison, without expansion of the solid volume, the reaction would stop when the final porosity approaches 0 (assuming all pores are connected) at around 70% conversion of CaO to $Ca(OH)_2$ for samples with initial porosity of 38%.

Table 1
Summary of the Experimental Conditions and Results for the Hydration Experiments

	σ (MPa)	T (°C)	r_0 (cm)	h_0 (cm)	V_0 (cm^3)	m_0 (g)	Φ_0	t (h)
#3	0.11	22	0.612 (5)	1.830 (5)	2.150 (41)	4.5294 (1)	0.371 (7)	20
#15[a]	0.11	22	0.609 (5)	1.690 (5)	1.966 (38)	4.0445 (1)	0.386 (7)	44
#B20	0.11	22	0.610 (5)	2.831 (5)	3.309 (60)	5.8124 (1)	0.476 (9)	41
#B3	0.11	22	0.612 (5)	1.830 (5)	2.150 (41)	3.9390 (1)	0.453 (9)	27
#6	0.4	22	0.613 (5)	1.379 (5)	1.625 (32)	3.4748 (1)	0.362 (7)	169
#11	0.4	22	0.613 (5)	1.822 (5)	2.147 (41)	4.1248 (1)	0.426 (8)	60
#12[b]	0.4	22	0.614 (5)	2.077 (5)	2.456 (46)	4.5848 (1)	0.443 (8)	24
#B21	0.4	22	0.610 (5)	2.420 (5)	2.829 (52)	5.2671 (1)	0.444 (8)	118
#B24	0.4	22	0.610 (5)	2.274 (5)	2.658 (49)	4.5457 (1)	0.490 (9)	137
#18	0.4	55	0.610 (5)	1.883 (5)	2.201 (42)	4.3306 (1)	0.413 (8)	21
#BS1[c]	0.99	22	0.610 (5)	2.398 (5)	2.803 (52)	4.45 (1)	0.53 (1)	767
#B22	4.2	22	0.610 (5)	2.179 (5)	2.547 (48)	4.9075 (1)	0.425 (8)	552
#7[b]	4.32	22	0.609 (5)	2.402 (5)	2.794 (52)	4.3729 (1)	0.53 (1)	400
#13	4.32	22	0.611 (5)	1.544 (5)	1.808 (35)	3.7070 (1)	0.388 (8)	613
#23[c]	4.32	55	0.610 (5)	1.883 (5)	2.201 (42)	4.3306 (1)	0.413 (8)	168
#17[c]	27.21	22	0.240 (5)	1.673 (5)	0.303 (14)	0.5200 (1)	0.49 (2)	2081

Note. All experiments reported in this table were performed with CaO powder produced after 2 hr of decarbonation of $CaCO_3$ at 850 °C. Drying process after the experiment is either 1 hr at 100 °C under vacuum (100 v) or 1 hr at 200 °C (200). σ = axial load; T = temperature; r = radius; h = height; V = volume; m = weight; Φ = porosity, subscripts 0 and f are for initial and final, respectively; t = duration of the experiments. The limits of precision (in brackets) are given in terms of the smallest unit reported: For example, 0.612 (5) and 2.150 (41) represent 0.612 ± 0.005 and 2.150 ± 0.041, respectively.
[a]The sample was lost during the extraction because it was too friable—reaction extent was approximately equal to 100%. [b]Samples lost during the drying process; % $Ca(OH)_2$ is calculated from wet weight. [c]The calculated % $Ca(OH)_2$ was initially higher than 100%. We corrected it to 100% and back-calculated m_f. [d]See Text S1 in the supporting information for details on calculations.

As can be seen in Figure 2, the strain, ε, exhibits a power law relationship with time,

$$\varepsilon = k_1 \cdot t^m, \tag{5}$$

with m = 0.38–0.72. The derivative of equation (5) as a function of time is

$$\dot{\varepsilon} = m k_1 \cdot t^{m-1}. \tag{6}$$

There is no systematic correlation between m and the applied load (σ).

Figure 2b illustrates that observed strain rates are all positive, though decreasing with time. Below, we will show that m is most likely ~0.5, so

$$\dot{\varepsilon} = 0.5 k_1 \frac{1}{\sqrt{t}}. \tag{7}$$

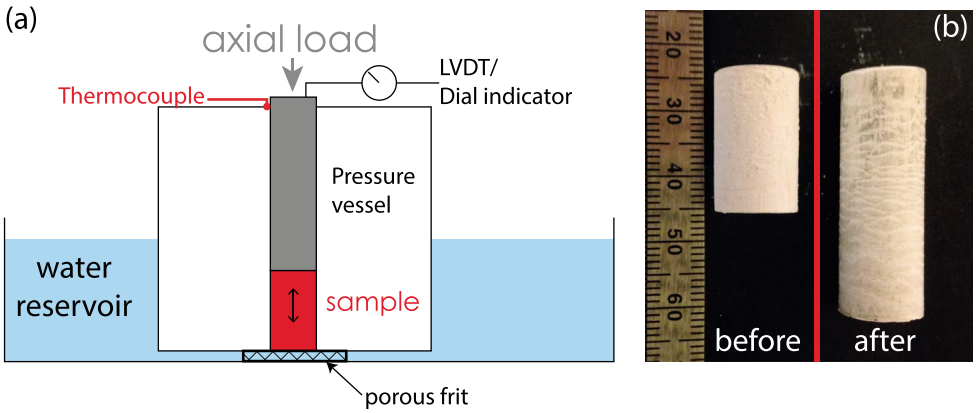

Figure 1. (a) Schematic of the experiments (not to scale). Internal diameter of the die was either 12.7 or 5 mm (run #17; Table 1). (b) Picture of the cold-pressed cylinder before and after hydration experiment with a uniaxial pressure of 0.4 MPa at 55 °C (run #18). The scale is in millimeters. LVDT = linear variable differential transformer.

Table 1 (*continued*)

	Drying (°C)	r_f (cm)	h_f (cm)	V_f (cm^3)	m_f (g)	% Ca(OH)$_2$[d]	Φ_f (bulk)[d]	Φ_f (Ca(OH)$_2$)[d]
#3	100 v	0.612 (10)	6.130 (10)	7.28 (19)	5.97 (5)	99.0 (34)	0.634 (71)	0.633 (93)
#15[a]	100 v	—	—	—	—	100.0	0.647	0.647
#B20	200	0.616 (10)	4.630 (10)	5.41 (14)	7.50 (5)	90.2 (27)	0.408 (40)	0.401 (53)
#B3	100 v	0.619 (10)	3.691 (10)	4.44 (12)	5.01 (5)	84.2 (40)	0.532 (75)	0.55 (10)
#6	100 v	0.613 (10)	2.319 (10)	2.73 (8)	4.59 (5)	99.9 (45)	0.247 (35)	0.247 (47)
#11	100 v	0.613 (10)	2.685 (10)	3.16 (9)	5.30 (5)	88.4 (38)	0.236 (31)	0.211 (38)
#12[b]	100 v	0.614 (10)	2.750 (10)	3.25 (9)	5.97 (5)	<74.0	>0.308 (36)	>0.26 (4)
#B21	200	0.616 (10)	3.878 (10)	4.62 (12)	6.84 (5)	93.1 (30)	0.358 (38)	0.35 (5)
#B24	200	0.616 (10)	3.266 (10)	3.89 (11)	5.86 (5)	89.8 (34)	0.358 (43)	0.343 (56)
#18	200	0.610 (10)	3.583 (10)	4.19 (12)	5.72 (5)	99.6 (36)	0.389 (46)	0.389 (60)
#BS1[c]	200	0.612 (10)	3.133 (10)	3.69 (10)	5.88 (5)	100.0 (35)	0.285 (33)	0.285 (44)
#B22	200	0.616 (10)	3.030 (10)	3.61 (10)	6.30 (5)	88.6 (32)	0.260 (30)	0.239 (37)
#7[b]	100 v	0.613 (10)	2.761 (10)	3.26 (9)	5.56 (5)	<82.2	>0.306 (40)	>0.257 (45)
#13	100 v	0.611 (10)	1.991 (10)	2.33 (7)	4.68 (5)	81.5 (42)	0.179 (28)	0.132 (38)
#23[c]	200	0.610 (10)	2.723 (10)	3.18 (9)	5.72 (5)	100.0 (36)	0.194 (23)	0.194 (31)
#17[c]	200	0.240 (10)	1.800 (10)	0.33 (2)	0.69 (5)	100.0 (30)	0.054 (44)	0.054 (65)

3.2. Strain Rate Proportional to the Square Root of Time

Second, the evolution of strain with axial load (Figure 3) is best fit by a power law:

$$k_1 = k_2 \cdot \sigma^{-\alpha}. \tag{8}$$

Thus, one can derive a flow law

$$\dot{\varepsilon} = \frac{0.5\, k_2}{\sigma^{\alpha}\sqrt{t}}. \tag{9}$$

By combining equations (5), (8), and (9), we obtain an alternative flow law in terms of axial load and strain rather than axial load and time:

$$\dot{\varepsilon} = \frac{0.5 k_2^2}{\sigma^{2\alpha}} \cdot \frac{1}{\varepsilon}. \tag{10}$$

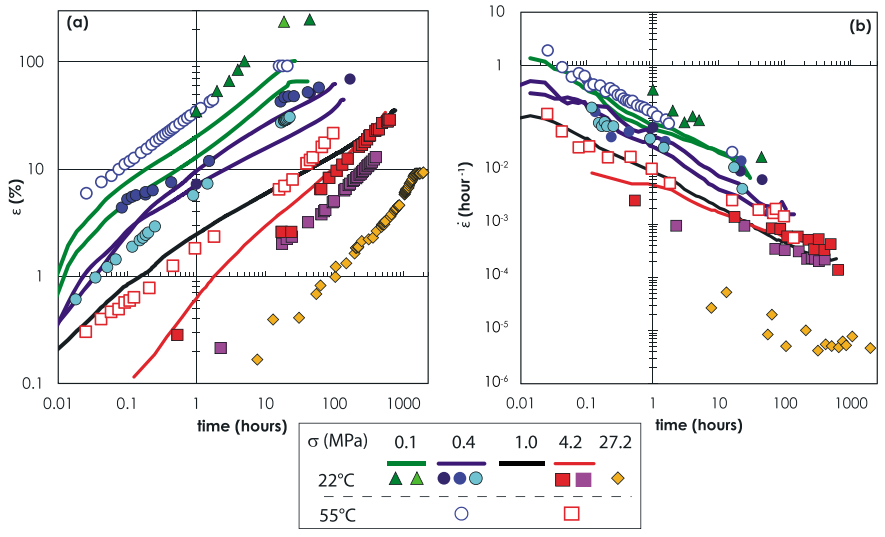

Figure 2. Evolution of the volumetric strain, $\varepsilon = \Delta V/V$ (a), and of the strain rate, $\dot{\varepsilon}$ (b), as a function of time under uniaxial loads, σ, between 0.1 and 27.2 MPa (Table S3). Experiments performed at 22 °C are represented with solid lines (recorded with LVDT) and solid symbols (recorded with dial indicator). Experiments performed at 55 °C are represented with open symbols (recorded with dial indicator). Strains are reported for displacements larger than the accuracy of the dial indicator (±0.001″).

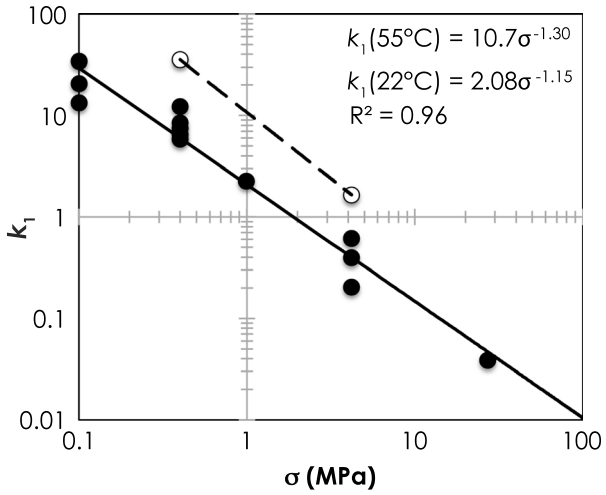

Figure 3. Strain at a time of 1 hr, k_1, versus stress, σ, for experiments at 22 °C (filled circles) and 55 °C (open circles). The solid line is the best fit to the 22 °C data. The dashed line connects the two data points at 55 °C.

3.3. Final Porosity Correlated With Uniaxial Load

Third, the final porosity in the experimental run products varies as a function of uniaxial load (Figure 4), with smaller final porosities at higher loads.

3.4. Possible Explanation for Variation in Replicated Experiments

We did not find a systematic explanation for sample-to-sample variation in replicated experiments. The scatter may be due to a combination of the size of the initial cylinder, the initial porosity, variable lubrication between the sample cylinder and the steel die, and perhaps the amount of impurities in the starting material.

4. Discussion

4.1. Flow Law

Using Washburn's equation (1921) for capillary rise in vertical cylindrical tubes and a capillary radius of 10 μm, we estimated that water would rise up to the top of a 4- to 6-cm cylinder in ~15–25 hr. This value is of the same order of magnitude than duration of the experiments at 0.1 MPa (Figure 2a; Table 1). In comparison, the CaO hydration reaction is fast, 2–3 min for highly reactive lime to reach full hydration (Miller, 1960). Hence, evolution of the volumetric strain with time (equation (5)) is primarily controlled by the absorption of water in the CaO cylinder via capillary infiltration. Infiltration in a porous medium by capillarity can be described as

$$I = S\cdot\sqrt{t} + A\cdot t, \tag{11}$$

where I is the liquid-front location, S is the sorptivity of the media, and A is a parameter that accounts for the contribution of gravity during vertical infiltration (Masoodi & Pillai, 2010; Philip, 1957). Because we observe that strain is approximately proportional to $\sqrt{t}$, and that porosity is related to the axial load, our data suggest that the strain rate is related to the sorptivity (Figures 2–4). Note that the design of our experiments differs from capillarity experiments, as the base of the CaO cylinder is partly below the water level (Figure 1a). Hence, the effect of gravity will be partly counterbalanced by the effect of the pressure at the entrance of the sample. Moreover, for such small samples, the gravitational effect is usually considered to be negligible (see Text S3 in the supporting information; Selker et al., 2007; Weisbrod et al., 2002). Hence, we can rewrite equation (11) as

$$\varepsilon = \frac{k_3}{h_0} S\cdot\sqrt{t} \text{ and } \frac{1}{\sqrt{t}} = \frac{k_3}{h_0} S \frac{1}{\varepsilon} \tag{12}$$

in which h_0 the initial height of the cylinder. Best fit values for $S_1 = k_3 S$ were calculated by minimizing the difference between experimental data and values predicted by equation (12).

Equation (12) explains 95% of the experimental variance and reproduces the observed strains with a standard error of estimate of 12% (see supporting information Figure S3), supporting our assumption that the volumetric strain is dominated by the sorptivity of the material.

In this analysis, S is assumed to be constant with time. Because the porosity is changing with time, and S is a function of permeability and porosity (see section 4.2), S should also be a function of time.

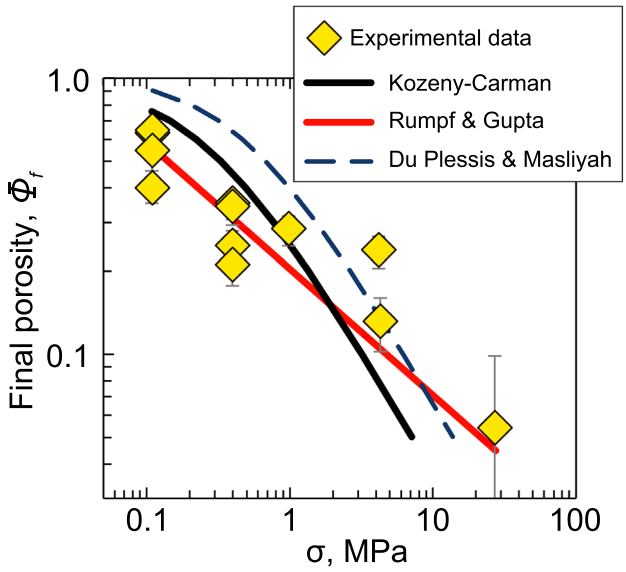

Figure 4. Final porosity Φ_f in the reacted portion of the charge as a function of σ for experiments at room temperature that reached more than 80% completion, compared to calculated porosity from the Kozeny-Carman equation (Carman, 1938, 1956; Koseny, 1956) and the models of Rumpf and Gupte (1971) and Du Plessis and Masliyah (1991), using $\alpha = 1.15$ (from fit to data in Figure 3) and grain diameter $d = 10$ μm. Best fit values were calculated by minimizing the sum of the squares between the experimental and model values. Error bars for Φ_f are based on propagation of uncertainties in sample length and weight (Table 1). When not visible, the error bar is smaller than the symbol.

Table 2
Equation Used for f(Φ) and Relationship Between σ and Φ

	$f(\Phi)$	$\sigma(\Phi)$
Kozeny-Carman equation	$\frac{\Phi^3}{(1-\Phi)^2}$	$k_8\left[\frac{d*(1-\Phi)^2}{\Phi^{2.5}}\right]^{1/2\alpha}$
Rumpf and Gupte	$\Phi^{5.5}$	$k_8\left[\frac{d}{\Phi^5}\right]^{1/2\alpha}$
Du Plessis and Masliyah	$\frac{\Phi\left[1-(1-\Phi)^{1/3}\right]\left[1-(1-\Phi)^{2/3}\right]}{(1-\Phi)^{4/3}}$	$k_8\left[\frac{d*(1-\Phi)^{4/3}}{\Phi^{0.5}\left[1-(1-\Phi)^{1/3}\right]\left[1-(1-\Phi)^{2/3}\right]}\right]^{1/2\alpha}$

However, expressions including the evolution of porosity with time do not significantly change the predicted strain evolution (see Text S4 in the supporting information).

Because the volumetric strain is dominated by the sorptivity of the material, we assume that equation (12) applies to our data and m in equation (5) is equal to 0.5. From equation (5)

$$k_1 = \frac{k_3}{h_0} S \tag{13}$$

and combining with equation (8)

$$\sigma^{-\alpha} = \frac{k_3 S}{k_2 h_0}, \text{so } \sigma^{\alpha} = \frac{k_2 h_0}{k_3 S} \text{ and } \sigma = k_4 [S]^{-1/\alpha}. \tag{14}$$

Thus, the combination of our observations and theoretical expressions allows us to relate sorptivity and axial load. Note that we can differentiate equation (12), and substitute $\frac{k_3}{h_0} S \frac{1}{\varepsilon}$ for $\frac{1}{\sqrt{t}}$ and $k_2 \cdot \sigma^{-\alpha}$ for $\frac{k_3}{h_0} S$ to obtain equation (10).

4.2. Relationship Between Axial Load and Porosity

In order to test our assumptions and develop a better understanding of the relationship between axial load and porosity (Figure 4), assuming one-dimensional fluid flow following Darcy's law, we used the following expression for S in a swelling porous media (Masoodi & Pillai, 2010):

$$S = \sqrt{\frac{4K\gamma\cos\theta}{\Phi_0 \eta R_c}} = \sqrt{\frac{k_5 K}{R_c}}, \tag{15}$$

where K is permeability, γ is surface tension of the liquid, θ is the contact angle, η is the liquid viscosity, and R_c is the capillary pore radius. Note that in equation (15), the effect of gravity is neglected. Simplified geometrical relationships between porosity, pore radius, and solid grain size (Ahern & Turcotte, 1979) yield

$$R_c{}^2 = k_6 \Phi d^2, \tag{16}$$

in which Φ is the porosity and d is the diameter of the solid grains. Several empirical and theoretical formulas have been developed to describe the permeability of a porous media as function of the porosity, which generally have the form

$$K = d^2 f(\Phi), \tag{17}$$

where $f(\phi)$ is a function of porosity (e.g., Masoodi & Pillai, 2010). Thus,

$$S = \sqrt{\frac{k_5 K}{R_c}} = \sqrt{\frac{k_5 d^2 f(\Phi)}{k_6{}^{0.5} \Phi^{0.5} d}} = k_7 \sqrt{\frac{f(\Phi)}{\Phi^{0.5} d}} \tag{18}$$

and

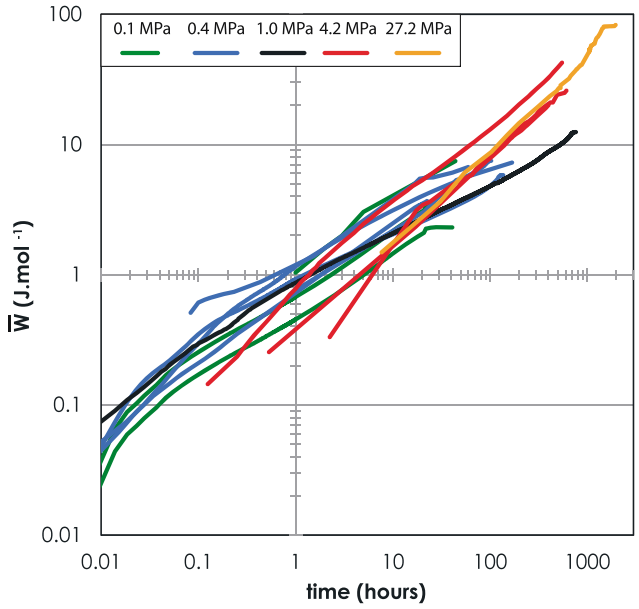

Figure 5. Evolution of the specific work $\overline{W}$ as a function of the time for experiments performed at room temperature.

$$\sigma = k_8 \left[\frac{\phi^{0.5} d}{f(\Phi)}\right]^{1/2\alpha} \tag{19}$$

This provides predictions of the relationship of porosity and axial load that can be compared to our observations of the final porosity in our experiments (Figure 4; Table 1). To predict porosity versus axial load using equation (19), we use three different functions for permeability as a function of Φ (Table 2): (1) the Kozeny-Carman equation (Carman, 1938, 1956; Koseny, 1956) for granular media consisting of arbitrary shaped particles, (2) Rumpf and Gupte's equation (1971) for packed spherical particles with porosity from 0.35 to 0.7, and (3) Du Plessis and Masliyah's model (1991) for a consolidated rock-like media with $\Phi > 0.1$.

Fixing α = 1.15 (based on the fit to data in Figure 3), and using a grain diameter of 10 μm, we found the best fit values for k_8 by minimizing the sum of the squares between experimental and model values. Rumpf and Gupte's empirical equation provides the best approximation of final porosity in the samples (Figure 4). The Kozeny-Carman equation is the most widely used relationship between porosity and permeability but has limited accuracy for the special case of sphere packing (Pan et al., 2001, and references therein). Du Plessis and Masliyah used the concept of a unit cell based on prismatic geometry (e.g., Du Plessis & Roos, 1994), whereas Rumpf and Gupte (1971) assume that grains are for packed spherical particles. Hence, our results suggest that CaO grains in our samples are better approximated by spherical particles.

4.3. Dependence of Strain on Axial Load

We have explored the relationship of expansion and sorptivity in the previous section to explain the power law relationship between strain and time at a given axial load (Figure 2). In this section, we discuss the negative, power law dependence between the strain and the axial stress.

In order to understand the decreasing strain at a given time with increasing uniaxial load (Figure 3; equation (12)), we first explored the role of pressure solution by performing a compaction experiment on wet portlandite with σ = 4.32 MPa (Text S5 in supporting information). If the reduction of the strain rate were due to compaction alone, we would be able to combine the power law relationship between strain and time at 0.1 MPa (Figure 2) with the compaction effect at σ = 4.32 MPa to reproduce the relationship between strain and time at 4.32 MPa. However, the compaction effect is negligible (see supporting information Figure S4; Zhang et al., 2002) and cannot be responsible for the decreasing strain at a given time with increasing uniaxial load. Instead, it is likely that our samples undergo relatively rapid compaction during the transformation from CaO to $Ca(OH)_2$.

An interesting clue is provided by considering the *work rate*. At a given time, the amount of work per mole, $\overline{W}$ (J/mol), produced by the system on its surroundings is

$$\overline{W} = \sigma \Delta V / n, \tag{20}$$

with n equal to the number of moles in the system. Figure 5 shows $\overline{W}$ as a function of time for experiments at room temperature. The 3-order-of-magnitude variation in strain at a given time (Figure 2a) is greatly reduced in Figure 5. Because $\Delta V/n$ is proportional to ε, the work done by the system—like the strain—is approximately proportional to the square root of time and independent of the applied axial load. In turn, filling of pore space reduces the porosity (Figure 4) and permeability, reducing the rate of capillary flow to the reaction front.

Since high load experiments required longer times for complete reaction, and the work rate is approximately independent of the load, the cumulative work during complete reaction must increase with increasing load (Figure 6). (Note that the total amount of energy produced as work in these experiments, ~1 to 70 J/mol for

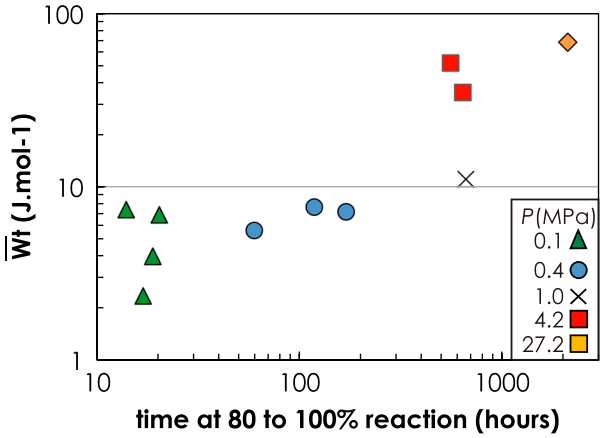

Figure 6. Total work, ($\overline{W_t}$), after 80% to 100% conversion of CaO to $Ca(OH)_2$.

reactions that were >80% complete, as shown in Figure 6, is orders of magnitude smaller than the available chemical potential energy from complete conversion of CaO to $Ca(OH)_2$ with $\Delta G_r = -57$ kJ/mol). We infer that most of the energy of reaction is consumed via dissipation processes such as frictional heating, thermal diffusion, and perhaps infinitesimal radial strain in the steel die around the sample cylinder. Interestingly, however, all of these dissipation mechanisms should probably be larger at larger loads over longer times, whereas our observations suggest that dissipation is less important at high loads and long durations.

4.4. Temperature Dependence

In Figures 2 and 3, experiments performed at 22 °C (room temperature) and 55 °C show displaced, broadly parallel relationships between strain and time, and between strain at a given time and σ, suggesting that k_1 in equations (5) and (6) (and consequently k_2; equation (8)) are temperature dependent. The strain after 1 hr, at a given uniaxial load, is about twice as large at 55 °C than in the 22 °C experiments. If the strain rate is directly proportional to the reaction rate, the calculated activation energy of the reaction in equation (3) is $Ea \sim 66$ kJ/mol (Figure S5) consistent with the range of 58.2 to 83.5 kJ/mol for the hydration of CaO reported in the literature (Schaube et al., 2012). Hence, our results not only suggest that higher temperatures increase the reaction rates but also that a faster reaction rate promotes faster fluid transport up the cylinder, perhaps by creating a more effective sink for H_2O at the reaction front and thus faster capillary flow. However, we should note that the increase of the reaction rate with increasing temperature will only apply far from the equilibrium temperature (i.e., 505 °C at 0.1-MPa H_2O partial pressure; Schaube et al., 2012). Schaube et al. (2012) observed a peak in reaction rate between 130 and 430 °C.

5. Summary

Because our reactive samples can still expand vertically under an axial load of 27 MPa, we can assume that samples would also expand against an isotropic confining stress equal to the axial load. This is consistent with experiments on CaO hydration by Wolterbeek et al. (2017), who estimated a maximum crystallization pressure of 153 MPa. Hence, full CaO hydration can be achieved while maintaining a finite porosity (and permeability) at depths extending to a few kilometers (using a crustal density of 2,700 kg/m^3). In our experimental geometry, fluid transport via sorption is rate limiting step in expansion during hydration of CaO to $Ca(OH)_2$. Increasing temperature may promote faster capillary flow as well as increased reaction rates at depth. Finally, the pressure of crystallization of $Ca(OH)_2$ exceeds the tensile strength of most igneous rocks at this depth. Hence, CaO hydration produces a stress sufficiently high to generate fractures at depths relevant for CO_2 sequestration, geothermal power generation, and shale gas extraction. However, in our experiments, strain and strain rate exhibit negative, power law dependence on axial load, suggesting that confining pressure—and hence burial depth—may exert a significant control on reaction rates and fluid transport and might limit the ability of the hydration reaction to generate stress and induce fractures.

Acknowledgments
This study has benefited from discussions with Marc Spiegelman, Greg Hirth, Misun Kang, and Rob Skarbek. Special thanks are due to Dave Walker and Ted Koczynski for their input on the experimental design. We thank two anonymous reviewers for their comments. This study also benefited from constructive comments from Erik Rybacki, Uli Faul, and an anonymous reviewer on a previous version of the manuscript. Data generated during this study are included in this published article and its supporting information files. This work was supported by the National Science Foundation grants EAR-1520732 and EAR-1516300 and a RISE (Research Initiatives in Science and Engineering) grant from Columbia University.

References

Ahern, J. L., & Turcotte, D. L. (1979). Magma migration beneath a mid-ocean ridge. *Earth and Planetary Science Letters*, *45*(1), 115–122. https://doi.org/10.1016/0012-821X(79)90113-4

Attewell, P. B., & Farmer, I. W. (1976). *Principles of engineering geology* (p. 1045). London: Chapman and Hall.

Borgwardt, R. H. (1989). Sintering of nascent calcium oxide. *Chemical Engineering Science*, *44*(1), 53–60.

Cai, M. (2010). Practical estimates of tensile strength and Hoek-Brown strength parameter m_i of brittle rocks. *Rock Mechanics and Rock Engineering*, *43*(2), 167–184. https://doi.org/10.1007/s00603-009-0053-1

Carlson, R. L., & Miller, D. J. (2003). Mantle wedge water contents estimated from seismic velocities in partially serpentinized peridotites. *Geophysical Research Letters*, *30*(5), 1250. https://doi.org/10.1029/2002GL016600

Carman, P. C. (1938). The determination of the specific surface of powders. *Journal of the Society of Chemical Industry*, *57*, 225–234.

Carman, P. C. (1956). *Flow of gases through porous media*. London: Butterworths Scientific Publications.

Coussy, O. (2006). Deformation and stress from in-pore drying-induced crystallization of salt. *Journal of the Mechanics and Physics of Solids*, *54*(8), 1517–1547. https://doi.org/10.1016/j.jmps.2006.03.002

Craft, K. L., & Lowell, R. P. (2009). A boundary layer model for submarine hydrothermal heat flows at on-axis and near-axis regions. *Geochemistry, Geophysics, Geosystems*, *10*, Q12012. https://doi.org/10.1029/2009GC002707

Derluyn, H., Moonen, P., & Carmeliet, J. (2014). Deformation and damage due to drying-induced salt crystallization in porous limestone. *Journal of the Mechanics and Physics of Solids*, *63*, 242–255. https://doi.org/10.1016/j.jmps.2013.09.005

Dessert, C., Dupré, B., Gaillardet, J., François, L. M., & Allègre, C. J. (2003). Basalt weathering laws and the impact of basalt weathering on the global carbon cycle. *Chemical Geology*, *202*(3-4), 257–273. https://doi.org/10.1016/j.chemgeo.2002.10.001

Du Plessis, J. P., & Masliyah, J. H. (1991). Flow through isotropic granular porous media. *Transport in Porous Media*, *6*(3), 207–221. https://doi.org/10.1007/bf00208950

Du Plessis, J. P., & Roos, L. I. (1994). Predicting the hydrodynamic permeability of sandstone with a pore-scale model. *Journal of Geophysical Research*, *99*(B10), 19,771–19,776. https://doi.org/10.1029/94JB01748

Espinosa-Marzal, R. M., & Scherer, G. W. (2010). Mechanisms of damage by salt. *Geological Society of London, Special Publication*, *331*(1), 61–77. https://doi.org/10.1144/SP331.5

Fletcher, R. C., Buss, H. L., & Brantley, S. L. (2006). A spheroidal weathering model coupling porewater chemistry to soil thicknesses during steady-state denudation. *Earth and Planetary Science Letters*, *244*(1-2), 444–457. https://doi.org/10.1016/j.epsl.2006.01.055

Fletcher, R. C., & Merino, E. (2001). Mineral growth in rocks: Kinetic-rheological models of replacement, vein formation, and syntectonic crystallization. *Geochimica et Cosmochimica Acta*, *65*(21), 3733–3748. https://doi.org/10.1016/S0016-7037(01)00726-8

Ghofrani, R., & Plack, H. (1993). CaO- and/or MgO-swelling cements: A key for providing a better annular sealing? SPE/IADC Drilling Conference. *Society of Petroleum Engineers*. https://doi.org/10.2118/25697-MS

Gorman, P. J., Kerrick, D. M., & Connolly, J. A. D. (2006). Modeling open system metamorphic decarbonation of subducting slabs. *Geochemistry, Geophysics, Geosystems*, *7*, Q04007. https://doi.org/10.1029/2005GC001125

Haynes, W. M. (2011). *CRC handbook of chemistry and physics* (92nd ed., p. 4.55). Boca Raton, FL: CRC Press. 1439855110

Hirauchi, K., Fukushima, K., Kido, M., Muto, J., & Okamoto, A. (2016). Reaction-induced rheological weakening enables oceanic plate subduction. *Nature Communications*, *7*, 12550. https://doi.org/10.1038/ncomms12550

Jamtveit, B., Putnis, C. V., & Malthe-Sørenssen, A. (2009). Reaction induced fracturing during replacement processes. *Contributions to Mineralogy and Petrology*, *157*(1), 127–133. https://doi.org/10.1007/s00410-008-0324-y

Kelemen, P. B., & Hirth, G. (2012). Reaction-driven cracking during retrograde metamorphism: Olivine hydration and carbonation. *Earth and Planetary Science Letters*, *345–348*, 81–89. https://doi.org/10.1016/j.epsl.2012.06.018.16

Kelemen, P. B., & Manning, C. E. (2015). Reevaluating carbon fluxes in subduction zones, what goes down, mostly comes up. *Proceedings of the National Academy of Sciences*, *112*(30), E3997–E4006. https://doi.org/10.1073/pnas.1507889112

Kelemen, P. B., & Matter, J. (2008). In situ carbonation of peridotite for CO_2 storage. *Proceedings of the National Academy of Sciences*, *105*(45), 17,295–17,300. https://doi.org/10.1073/pnas.0805794105

Kelemen, P. B., Matter, J., Streit, E. E., Rudge, J. F., Curry, W. B., & Blusztajn, J. (2011). Rates and mechanisms of mineral carbonation in peridotite: Natural processes and recipes for enhanced, in situ CO_2 capture and storage. *Annual Review of Earth and Planetary Sciences*, *39*(1), 545–576. https://doi.org/10.1146/annurev-earth-092010-152509

Kelemen, P. B., Savage, H., & Hirth, G. (2013). Reaction-driven cracking during mineral hydration, carbonation and oxidation. *Fifth Biot Conference on Poromechanics*. Vienna, Austria. https://doi.org/10.1061/9780784412992.099

Kornprobst, T., & Plank, J. (2013). Synthesis and properties of magnesium carbonate xerogels and aerogels. *Journal of Non-Crystalline Solids*, *361*, 100–105. https://doi.org/10.1016/j.jnoncrysol.2012.10.023

Koseny, J. (1956). Capillary transport of water in the soil. *Sitzungbererichte the Akadamie of Sciences Tung in Wine Abeilung*, *136*, 271–301.

Kuleci, H., Ulven, O. I., Rybacki, E., Wunder, B., & Abart, R. (2017). Reaction-induced fracturing in a hot pressed calcite-periclase aggregate. *Journal of Structural Geology*, *94*, 116–135. https://doi.org/10.1016/j.jsg.2016.11.009

Kumazawa, M., & Anderson, O. L. (1969). Elasti moduli, pressure derivatives, and temperature derivatives of single-crystal olivine and single-crystal forsterite. *Journal of Geophysical Research*, *74*(25), 5961–5972. https://doi.org/10.1029/JB074i025p05961

Lee, B. Y., & Kurtis, K. E. (2017). Effect of pore structure on salt crystallization damage of cement-based materials: Consideration of w/b and nanoparticle use. *Cement and Concrete Research*, *98*, 61–70. https://doi.org/10.1016/j.cemconres.2017.04.002

Lumb, P. (1983). Engineering properties of fresh and decomposed igneous rocks from Hong Kong. *Engineering Geology*, *19*(2), 81–94. https://doi.org/10.1016/0013-7952(83)90027-3

Masoodi, R., & Pillai, K. M. (2010). Darcy's law-based model for wicking in paper-like swelling porous media. *AIChE Journal*, *56*, NA–2267. https://doi.org/10.1002/aic.12163

Matter, J. M., Stute, M., Snæbjörnsdottir, S. Ó., Oelkers, E. H., Gislason, S. R., Aradottir, E. S., et al. (2016). Rapid carbon mineralization for permanent disposal of anthropogenic carbon dioxide emissions. *Science, 352*, 1312–1314. https://doi.org/10.1126/science.aad8132

McGovern, P. J., & Schubert, G. (1989). Thermal evolution of the Earth: Effects of volatile exchange between atmosphere and interior. *Earth and Planetary Science Letters*, *96*(1-2), 27–37. https://doi.org/10.1016/0012-821X(89)90121-0

Miller, T. C. (1960). *A study of the reaction between calcium oxide and water* (p. 42). Washington, DC: National Lime Association.

Noiriel, C., Renard, F., Doan, M.-L., & Gratier, J.-P. (2010). Intense fracturing and fracture sealing induced by mineral growth in porous rocks. *Chemical Geology*, *269*(3-4), 197–209. https://doi.org/10.1016/j.chemgeo.2009.09.018

Osselin, F., Fabbri, A., Fen-Chong, T., Dangla, P., Pereira, J. -M., & Lassin, A. (2014). Stress from NaCl crystallisation by carbon dioxide injection in aquifers. *Environmental Geotechnics*, *2*(5), 280–291. https://doi.org/10.1680/envgeo.13.00057

Ostapenko, G. T., & Yaroshenko, N. S. (1975). Excess pressure on solid phases generated by hydration (experimental data on hydration of plaster of Paris and lime). *Geochemistry International*, 12.

Pan, C., Hilpert, M., & Miller, C. T. (2001). Pore-scale modeling of saturated permeabilities in random sphere packings. *Physical Review E*, *64*(6), 066702. https://doi.org/10.1103/PhysRevE.64.066702

Philip, J. R. (1957). The theory of infiltration: 4. Sorptivity and algebraic infiltration equations. *Soil Science*, *84*(3), 257–264. https://doi.org/10.1097/00010694-195709000-00010

Putnis, A. (2009). Mineral replacement reactions. *Reviews in Mineralogy and Geochemistry*, *70*(1), 87–124. https://doi.org/10.2138/rmg.2009.70.3

Rahman, S. F., & Grasley, Z. C. (2017). The significance of pore liquid pressure and disjoining pressure on the desiccation shrinkage of cementitious materials. *International Journal of Advances in Engineering Sciences and Applied Mathematics*, *9*(2), 87–96. https://doi.org/10.1007/s12572-017-0186-5

Roland, E., Behn, M. D., & Hirth, G. (2010). Thermal-mechanical behavior of oceanic transform faults: Implications for the spatial distribution of seismicity. *Geochemistry, Geophysics, Geosystems*, *11*, Q07001. https://doi.org/10.1029/2010GC003034

Røyne, A., & Jamtveit, B. (2015). Pore-scale controls on reaction-driven fracturing. *Reviews in Mineralogy and Geochemistry*, *80*(1), 25–44. https://doi.org/10.2138/rmg.2015.80.02

Rumpf, H. C. H., & Gupte, A. R. (1971). Einflüsse der Porosität und Korngrößenverteilung im Widerstandsgesetz der Porenströmung. *Chemie Ingenieur Technik*, *43*(6), 367–375. https://doi.org/10.1002/cite.330430610

Schaube, F., Koch, L., Wörner, A., & Müller-Steinhagen, H. (2012). A thermodynamic and kinetic study of the de- and rehydration of $Ca(OH)_2$ at high H_2O partial pressures for thermo-chemical heat storage. *Thermochimica Acta*, *538*, 9–20. https://doi.org/10.1016/j.tca.2012.03.003

Schmidt, M. W., & Poli, S. (1998). Experimentally based water budgets for dehydrating slabs and consequences for arc magma generation. *Earth and Planetary Science Letters*, *163*(1-4), 361–379. https://doi.org/10.1016/S0012-821X(98)00142-3

Schultz, R. A. (1995). Limits on strength and deformation properties of jointed basaltic rock masses. *Rock Mechanics and Rock Engineering*, *28*(1), 1–15. https://doi.org/10.1007/BF01024770

Selker, J. S., Niemet, M., McDuffie, N. G., Gorelick, S. M., & Parlange, J.-Y. (2007). The local geometry of gas injection into saturated homogeneous porous media. *Transport in Porous Media*, *68*(1), 107–127. https://doi.org/10.1007/s11242-006-0005-0

Shahidzadeh-Bonn, N., Rafaï, S., Bonn, D., & Wegdam, G. (2008). Salt crystallization during evaporation: Impact of interfacial properties. *Langmuir*, *24*(16), 8599–8605. https://doi.org/10.1021/la8005629

Shin, H. G., Kim, H., Kim, Y. N., & Lee, H. S. (2009). Effect of reactivity of quick lime on the properties of hydrated lime sorbent for SO2 removal. *Journal of Materials Science and Technology*, *25*, 329–332.

Skarbek, R. M., Savage, H. M., Kelemen, P. B., & Yancopoulos, D. (2018). Competition between crystallization-induced expansion and creep compaction during gypsum formation, and implications for serpentinization. *Journal of Geophysical Research: Solid Earth*, *123*, 5372–5393. https://doi.org/10.1029/2017JB015369

Sobolev, A. V., & Chaussidon, M. (1996). H_2O concentrations in primary melts from supra-subduction zones and mid-ocean ridges: Implications for H_2O storage and recycling in the mantle. *Earth and Planetary Science Letters*, *137*(1-4), 45–55. https://doi.org/10.1016/0012-821X(95)00203-O

Steiger, M. (2005). Crystal growth in porous materials—II: Influence of crystal size on the crystallization pressure. *Journal of Crystal Growth*, *282*(3-4), 470–481. https://doi.org/10.1016/j.jcrysgro.2005.05.008

Taylor, H. F. W. (1997). *Cement chemistry*, (2nd ed.). London: Thomas Telford Publishing. https://doi.org/10.1680/cc.25929

Van Avendonk, H. J. A., Holbrook, W. S., Lizarralde, D., & Denyer, P. (2011). Structure and serpentinization of the subducting Cocos plate offshore Nicaragua and Costa Rica. *Geochemistry, Geophysics, Geosystems*, *12*, Q06009. https://doi.org/10.1029/2011GC003592

Van Noort, R., Wolterbeek, T. K. T., Drury, M. R., Kandianis, M. T., & Spiers, C. J. (2017). The force of crystallization and fracture propagation during in-situ carbonation of peridotite. *Minerals*, *7*(10), 190, 31 https://doi.org/10.3390/min7100190

Washburn, E. W. (1921). The dynamics of capillary flow. *Physical Review*, *17*(3), 273–283. https://doi.org/10.1103/PhysRev.17.273

Weisbrod, N., Niemet, M. R., & Selker, J. S. (2002). Imbibition of saline solutions into dry and prewetted porous media. *Advances in Water Resources*, *25*(7), 841–855. https://doi.org/10.1016/S0309-1708(02)00038-6

Wolterbeek, T. K. T., van Noort, R., & Spiers, C. J. (2017). Reaction-driven casing expansion: Potential for wellbore leakage mitigation. *Acta Geotechnica*. https://doi.org/10.1007/s11440-017-0533-5

Zhang, X., Salemans, J., Peach, C. J., & Spiers, C. J. (2002). Compaction experiments on wet calcite powder at room temperature: Evidence for operation of intergranular pressure solution. *Geological Society - Special Publications*, *200*(1), 29–39. https://doi.org/10.1144/GSL.SP.2001.200.01.02

Zheng, X., Cordonnier, B., Zhu, W., Renard, F., & Jamtveit, B. (2018). Effects of confinement on reaction-induced fracturing during hydration of periclase. *Geochemistry, Geophysics, Geosystems*, *19*. https://doi.org/10.1029/2017GC007322

Zhu, W., Fusseis, F., Lisabeth, H., Xing, T., Xiao, X., De Andrade, V., & Karato, S. (2016). Experimental evidence of reaction-induced fracturing during olivine carbonation. *Geophysical Research Letters*, *43*, 9535–9543. https://doi.org/10.1002/2016GL070834